A&A 666, A18 (2022)
https://doi.org/10.1051/0004-6361/202244148

Astronomy & Astrophysics

Constraining the overcontact phase in massive binary evolution

II. Period stability of known O+O overcontact systems

Michael Abdul-Masih[1], Ana Escorza[1], Athira Menon[2,3,4], Laurent Mahy[5], and Pablo Marchant[6]

[1] European Southern Observatory, Alonso de Cordova 3107, Vitacura, Casilla 19001, Santiago de Chile, Chile
e-mail: michael.abdul-masih@eso.org
[2] Instituto de Astrofísica de Canarias, 38 200 La Laguna, Tenerife, Spain
[3] Universidad de La Laguna, Universidad de La Laguna, 38 205 La Laguna, Tenerife, Spain
[4] Argelander Institut für Astronomie, Universität Bonn, Auf dem Hügel 71, 53121 Bonn, Germany
[5] Royal Observatory of Belgium, Avenue Circulaire/Ringlaan 3, B1180 Brussels, Belgium
[6] Institute of Astronomy, KU Leuven, Celestijnenlaan 200 D, 3001 Leuven, Belgium

Received 30 May 2022 / Accepted 1 August 2022

ABSTRACT

Context. Given that mergers are often invoked to explain many exotic phenomena in massive star evolution, understanding the evolutionary phase directly preceding a merger, the overcontact phase, is of crucial importance. Despite this, large uncertainties exist in our understanding of the evolution of massive overcontact binaries.
Aims. We aim to provide robust observational constraints on the future dynamical evolution of massive overcontact systems by measuring the rate at which the periods change for a sample of six such objects. Furthermore, we aim to investigate whether the periods of unequal-mass systems show higher rates of change than their equal mass counterparts, as theoretical models predict.
Methods. Using archival photometric data from various ground- and space-based missions covering up to ∼40 years, we measure the periods of each system over several smaller time spans. We then fit a linear regression through the measured periods to determine the rate at which the period is changing over the entire data set.
Results. We find that all of the stars in our sample have very small period changes and that there does not seem to be a correlation with the mass ratio. This implies that the orbital periods for these systems are stable on the nuclear timescale, and that the unequal-mass systems may not equalize as expected.
Conclusions. When comparing our results with population synthesis distributions, we find large discrepancies between the expected mass ratios and period stabilities. We find that these discrepancies can be mitigated to a degree by removing systems with shorter initial periods, suggesting that the observed sample of overcontact systems may originate from binary systems with longer initial orbital periods.

Key words. binaries: close – stars: massive – stars: evolution – techniques: photometric

1. Introduction

With a binary fraction of ∼100%, the presence of a companion plays a crucial role in the evolution of massive stars (e.g., Sana et al. 2011; Duchêne & Kraus 2013; Moe & Di Stefano 2017). Throughout their lives, it is expected that approximately 70% of massive stars will interact with a companion (e.g., Sana et al. 2012) and of those that do, 40% (24% of all massive stars) will evolve through an overcontact phase (e.g., Pols 1994; Wellstein et al. 2001; de Mink et al. 2007). Nevertheless, very few massive overcontact systems are known (see, e.g., Leung & Schneider 1978; Popper 1978; Hilditch et al. 2005; Penny et al. 2008; Lorenzo et al. 2014, 2017; Almeida et al. 2015; Martins et al. 2017; Mahy et al. 2020a; Janssens et al. 2021).

Despite the rarity of these systems, the overcontact phase can be of crucial importance in the evolution of massive binary systems. The unique geometry and strong binary interactions during this phase make the internal processes difficult to accurately constrain (see, e.g., Fabry et al. 2022). Depending on the treatment of these internal processes and the rate of mass transfer as a binary system first comes into contact, systems evolving through this phase can have drastically different end products. For example, objects such as magnetic massive stars (Schneider et al. 2019), Be stars (Shao & Li 2014), luminous blue variables (Justham et al. 2014; Smith et al. 2018), blue stragglers (Eggen & Iben 1989; Mateo et al. 1990) and peculiar Type-II supernovae such as SN-1987A (Podsiadlowski et al. 1992; Menon & Heger 2017; Urushibata et al. 2018) have all been postulated to be the direct result of massive binary mergers. Alternatively, if the conditions are right (i.e., efficient internal mixing), theoretical studies predict that overcontact systems may be able to avoid merging while on the main sequence, instead forming double black hole binary systems and eventually gravitational wave sources via the chemically homogeneous evolution pathway (de Mink & Mandel 2016; Mandel & de Mink 2016; Marchant et al. 2016; du Buisson et al. 2020; Riley et al. 2021).

An important question when considering the future evolution of a massive overcontact binary system is whether it is evolving on a nuclear timescale, which would imply that the system is relatively stable, or on a thermal timescale, implying that the system is unstable and will most likely either merge or separate

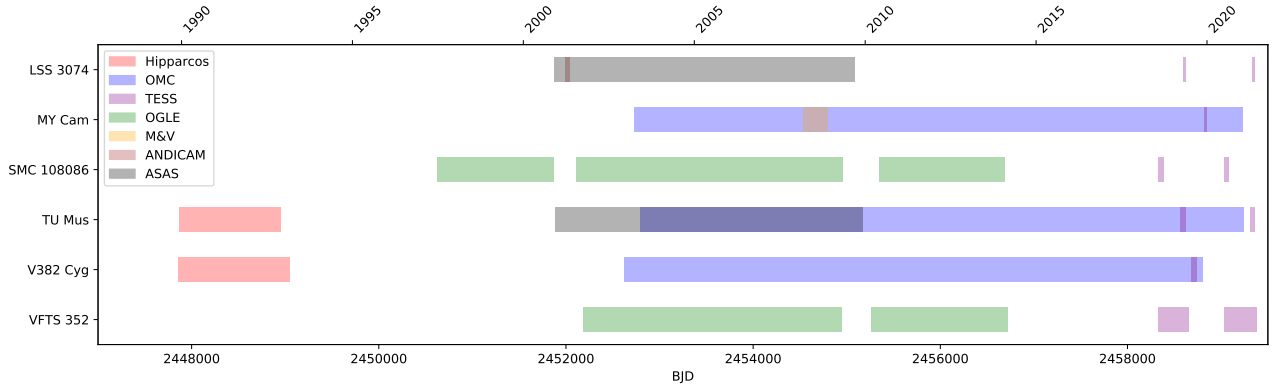

Fig. 1. Overview of the photometric data available for each object in our sample. Each color-shaded region corresponds to a different instrument or data set. Red indicates HIPPARCOS, blue indicates INTEGRAL-OMC, green indicates OGLE, black indicates ASAS, brown indicates ANDICAM, yellow indicates data from Lorenzo et al. (2014), and data from TESS are indicated in purple. We note that these ranges indicate the date ranges of the respective data sets, some of which are sporadic and without a regular cadence.

(Pols 1994). Due to their extremely short-lived nature, observing a thermal-timescale overcontact system is expected to be very unlikely, so it is often assumed that the known massive overcontact systems are evolving on the nuclear timescale. Theoretical studies focused on stable massive overcontact binaries indicate that these systems should very quickly equalize in mass, and then continue to evolve on a nuclear timescale (Marchant et al. 2016; Menon et al. 2021). Observationally; however, most of the known massive overcontact binaries are found in unequal-mass systems.

The discrepancy between the observed and expected mass ratios in combination with the lower than-expected number of known massive overcontact binaries when compared with predictions from population synthesis studies (e.g., Langer et al. 2020; Menon et al. 2021) leads to several interesting open questions. Is the contact phase less stable and therefore shorter-lived than we expect? Are we preferentially observing systems before they equalize in mass, or is our prediction that these systems equalize flawed? By investigating how the period changes over several years, we can begin to answer some of these questions.

In this paper we combine archival photometric data sets obtained over a long period of time to investigate the period stability of known massive overcontact systems. By determining how quickly the orbital period is changing, we can determine whether these systems are evolving on nuclear or thermal timescales. Further, we can determine whether these systems are in the process of equalizing in mass or if they are evolving as long-lived but unequal-mass overcontact binaries. In Sect. 2 we discuss our sample selection and the available photometry for each source as well as our data reduction techniques (when applicable). In Sect. 3 we detail our period determination procedure and how we calculate the period stability. We present our results in Sect. 4, and we discuss the implications of our findings in Sect. 5. Finally, Sect. 6 summarizes our findings and discusses future prospects.

2. Sample and observations

Since the goal of this investigation is to characterize the period change in massive overcontact systems, we selected our sample based on a set of criteria designed to ensure that we remove as many biases as possible. These four criteria are as follows.

First, the optimal solution for the system must be an overcontact configuration and further, this must have been determined via a combined photometric and radial velocity fit. Ensuring that the system is in an overcontact configuration is of the utmost importance since semidetached and detached systems with ellipsoidal deformations will have different period evolutions and will thus probe different physical effects than those that dominate during the overcontact phase.

Second, the system must not be in a confirmed triple or higher order multiple system unless we can ensure that the additional components are far enough from the binary such that they have a negligible effect on the dynamics of the system (see, e.g., Toonen et al. 2016). The presence of a nearby third object ($P_{\rm out} \lesssim 10$ yr for massive overcontact systems) is known to alter the period and orbital parameters of the inner binary system via von Zeipel–Kozai–Lidov (vZKL) oscillations (von Zeipel 1910; Kozai 1962; Lidov 1962). These perturbations could bias the period variation measurements and for this reason, these systems are excluded from our sample.

Third, if the photometric data of the system is contaminated with other periodic signals, the signature of the binary must be the dominant signal.

Fourth, both of the system's components must be main sequence O-type stars. This criterion is meant to ensure that the sample is as complete as possible in the given spectral range, while also limiting the sample size to a manageable amount.

With the above criteria, our final sample consists of six objects that are spread over different metallicity regimes, including the Milky Way and the Large and Small Magellanic Clouds. These systems and their available photometric data are discussed in detail below. An overview of the photometric data used for each target as well as the time bases that the different data sets cover is presented in Fig. 1. Additionally, the most relevant parameters to this study including the periods, mass ratios and fillout factors are summarized in Table 1.

For the purposes of this study, we define the primary as the currently more massive component and the mass ratio (q) as the mass of the secondary over the mass of the primary such that $q \leq 1$. The fillout factor, which is a measure of the degree to which a system is overfilling its Roche lobes, has several different definitions in the literature. Here, we adopt the definition of the fillout factor f from Mochnacki & Doughty (1972), which states

$$f = \frac{\Omega_{n,1} - \Omega_n}{\Omega_{n,1} - \Omega_{n,2}} + 1, \tag{1}$$

Table 1. Selected orbital parameters for each of the systems in our sample.

	$P_{\rm orb}$ [d]	M_1 [$M_\odot$]	M_2 [$M_\odot$]	q (M_1/M_2)	f	Reference
LSS 3074	2.1852	17.2 ± 1.4	14.8 ± 1.1	0.86 ± 0.04	1.05	Raucq et al. (2017)
MY Cam	1.1754514	37.7 ± 1.6	31.6 ± 1.4	0.84 ± 0.03	1.01	Lorenzo et al. (2014)
SMC 108086	0.8830987	16.9 ± 1.2	14.3 ± 1.7	0.85 ± 0.06	1.70	Hilditch et al. (2005)
TU Mus	1.387282	16.7 ± 0.4	10.4 ± 0.4	0.623 ± 0.009	1.12	Penny et al. (2008)
V382 Cyg	1.885545	26.1 ± 0.4	19.0 ± 0.3	0.727 ± 0.005	1.10	Martins et al. (2017)
VFTS 352	1.1241452	28.9 ± 0.3	28.6 ± 0.3	0.99 ± 0.10	1.28	Almeida et al. (2015)

Notes. The last column indicates the reference from which the orbital solutions were derived. We note that while the other parameters come directly from each of these papers, the fillout factors were calculated using Eq. (1) as described in Sect. 2.

where $\Omega_{n,1}$ and $\Omega_{n,2}$ denote the potential of the surface passing through L1 and L2, respectively, and Ω_n indicates the measured surface potential of the system. In this definition, an overcontact system has a fillout factor $1 < f < 2$, with higher fillout factors corresponding to systems in deeper contact. Since the degree of deformation for the systems in our sample are not presented in a consistent way throughout the literature, we compute the fillout factor according to the above definition for each object in our sample to ensure homogeneity.

2.1. LSS 3074

LSS 3074 was initially characterized as a contact system by Raucq et al. (2017) and is located in the Milky Way. With a fillout factor of 1.05, the system is just barely in contact; however, the photometric analysis strongly favors a contact configuration over a semidetached configuration. The period was measured to be 2.1852 days, making it the longest period system in our sample. This, in combination with its masses of 17.2 and 14.8 $M_\odot$, imply that it may be slightly more evolved than the rest of our sample. While the spectral types of both components appear to be solidly in the O-type regime, the anomalous combination of certain spectral features did not allow Raucq et al. (2017) to firmly determine a spectral type for each component.

The photometric data set for LSS 3074 consists of data from the All Sky Automated Survey (ASAS), data from A Novel Dual Imaging Camera (ANDICAM) and two sectors of data from the Transiting Exoplanet Survey Satellite (TESS). The data from ANDICAM were collected between March and May of 2001 and were observed in the Johnson B, V, R, and I bands (Raucq et al. 2017). The ASAS data were collected sporadically over a nine year period between 2000 and 2009 and were observed in the V band (Pojmanski 1997, 2002, 2003; Pojmanski & Maciejewski 2004, 2005; Pojmanski et al. 2005). Since LSS 3074 is a southern object, it was observed during the first and third year of TESS mission with data in sectors 11 and 38, respectively (Ricker et al. 2015). We note that there are also data from the International Gamma-Ray Astrophysics Laboratory Optical Monitoring Camera (INTEGRAL-OMC) available for the target; however, the quality of the light curve was not good enough to allow us to detect a statistically significant peak near the orbital frequency, so we do not include it in this analysis.

2.2. MY Cam

MY Cam is located in the Milky Way and was first characterized as a contact system by Lorenzo et al. (2014). With component masses of 37.7 and 31.6 and spectral types of O5.5 and O7, respectively, it is the most massive overcontact system currently known. Its period was measured to be ∼1.175 days and it has a mass ratio of 0.84. Of all of the systems in our sample, MY Cam has the lowest measured fillout factor at only 1.01, meaning that it just barely qualifies as an overcontact system.

The photometric data set for MY Cam consists of data from INTEGRAL-OMC and TESS as well as data from two private telescopes. The INTEGRAL-OMC data were observed in the Johnson V band and were collected sporadically over an ∼18 year time frame between 2003 and 2021 (Alfonso-Garzón et al. 2012). Unfortunately, only one sector of TESS data is available, which was observed in sector 19 during the second year of the TESS mission. In addition to these, photometric data were collected from two private telescopes during a six month period in 2008. These two telescopes were a Meade LX200 and a Vixen VISAC and observed in the Johnson R band (Lorenzo et al. 2014). Since the telescope and instrument names were not provided, we refer to this data set as M&V henceforth reflecting the telescope models from which the data were collected.

2.3. OGLE SMC-SC10 108086

OGLE SMC-SC10 108086 (SMC 108086 henceforth) was first characterized as a contact system by Hilditch et al. (2005), and as its name suggests, it is located in the Small Magellanic Cloud (SMC). The primary and secondary components have spectral types of O9 and O9.5, respectively, and their locations on the Hertzsprung–Russell diagram indicate that they are very close to the zero-age main sequence (Abdul-Masih et al. 2021). With a fillout factor of 1.7 and a period of around 0.88 days (Pawlak et al. 2016), it is both the deepest massive overcontact system currently known and the shortest period system in our sample. This, in combination with its mass ratio of 0.85, makes it an ideal test case for this investigation.

The photometric data set for SMC 108086 consists of both Optical Gravitational Lensing Experiment (OGLE) and TESS data. As part of the OGLE II, III, and IV campaigns, it was observed sporadically over a total time span of ∼16 years (Udalski et al. 1997, 2008, 2015; Szymanski 2005). While only I band data are available for OGLE II, it was observed in both the I- and V bands during OGLE III and IV. Being in the southern hemisphere, it was observed during the first and third year of TESS with a total of four sectors of data available (sectors 1, 2, 27, and 28).

2.4. TU Mus

Along with V382 Cyg, TU Mus was one of the first massive overcontact systems identified and is located in the Milky Way.

It was originally characterized as a contact system by Andersen & Grønbech (1975), and has been studied extensively since then (e.g., Stickland et al. 1995; Terrell et al. 2003; Linder et al. 2007; Qian et al. 2007; Penny et al. 2008). It has a period of around 1.387 days and a fillout factor of 1.12, and with a mass ratio of 0.623, it is the most unequal-mass system in our sample. While it is universally agreed upon that the primary is an O-type star, there is some ambiguity in the literature as to the status of the secondary; some sources claim that it is a late O-type star (e.g., Terrell et al. 2003; Penny et al. 2008) while others claim that its spectral type is early B (e.g., Sota et al. 2014; Maíz Apellániz et al. 2016). It is also important to note that Qian et al. (2007) found evidence of a third object gravitationally bound to the system, but given its long period (∼47 years) and low component mass, it is expected to have a negligible effect on the dynamics of the inner contact system. Based on the parameters of the system, the vZKL oscillations are expected to operate on timescales of ∼0.9 Myr (see Eq. (24) in Toonen et al. 2016)

The photometric data set for TU Mus consists of data from Hipparcos, ASAS, INTEGRAL-OMC, and TESS. The Hipparcos data (Perryman et al. 1997) were collected between December 1989 and November 1992, and were observed in the Hipparcos passband (Hp). The ASAS data were collected sporadically over a nine year period between December 2000 and December 2009 and were observed in the V band. The INTEGRAL-OMC data were collected in the Johnson V band between 2003 and 2021. Finally, there are four sectors of TESS data available, two sectors (11 and 12) in the first year and two sectors (37 and 38) in the third year of the TESS campaign.

2.5. V382 Cyg

V382 Cyg was first identified and characterized in the late 1970s (Cester et al. 1978; Popper 1978) and has been the subject of numerous studies since then (e.g., Popper & Hill 1991; Harries et al. 1997; Burkholder et al. 1997; Değirmenci et al. 1999; Qian et al. 2007; Yaşarsoy & Yakut 2013). Located in the Milky Way, the primary and secondary components have spectral types of O6.5 and O6, respectively. Recently, Martins et al. (2017) reanalyzed the system and updated the orbital parameters, reporting an orbital period of ∼1.89 days with a fillout factor of 1.10 and a mass ratio of 0.727. Despite its low fillout factor, recent spectroscopic observations of this system indicate potentially high levels of mixing between the two components, giving further evidence that the system is indeed in a contact configuration (Abdul-Masih et al. 2021). As with TU Mus, Qian et al. (2007) found evidence that V382 Cyg has a tertiary component, but its period and mass suggest that it is likely to have a negligible effect on the dynamics of the contact system with a vZKL oscillation timescale of ∼0.8 Myr. This was later confirmed by Yaşarsoy & Yakut (2013), who updated the period to be ∼43 years.

The photometric data set for V382 Cyg is composed of data from Hipparcos, INTEGRAL-OMC and TESS. The data from the Hipparcos Catalog were observed between October 1989 and February 1993 and were observed in the Hipparcos passband. The data from the INTEGRAL-OMC on the other hand were observed sporadically over a ∼18 year time frame between 2002 and 2019 and were observed in the Johnson V band. In addition to these, V382 Cyg was observed by TESS in sectors 14 and 15 during the second year of the TESS mission.

2.6. VFTS 352

VFTS 352 is located in the Large Magellanic Cloud (LMC) and was first characterized by Almeida et al. (2015). The nearly twin components (q = 0.99) have masses of ∼29 $M_\odot$ and have spectral types of O4.5 and O5.5, making it the earliest overcontact system currently known (Walborn et al. 2014; Almeida et al. 2015, 2017; Mahy et al. 2020a,b). Its high component masses, short period (∼1.124 days) and relatively high fillout factor (1.28) make it a promising candidate for a gravitational wave progenitor (de Mink & Mandel 2016; Mandel & de Mink 2016; Marchant et al. 2016; Abdul-Masih et al. 2019, 2020, 2021).

The photometric data set for VFTS 352 is composed of data from the OGLE III and IV campaigns as well as TESS. The data from OGLE III and IV were collected sporadically over a total time span of ∼13 years between 2001 and 2014 in both the I and V bands. Given its location in the LMC, VFTS 352 fell in TESS's continuous viewing zone, meaning that it was observed for the entirety of the first and third years.

2.7. Rejected systems

Several other O-type overcontact systems are known, but these were not included in our sample for various reasons. LY Aur is a known triple with vZKL oscillation timescales on the order of ∼0.2 Myr (Stickland et al. 1994; Zhao et al. 2014). Given the short oscillation timescale, we reject it from our sample. V729 Cyg is long period (∼6.6 days), evolved overcontact system that is no longer on the main sequence so it is not included (Antokhina et al. 2016). OGLE-SMC-ELC-4690 is thought to be a contact system, but no combined photometric and radial velocity fit has been performed on the object. Furthermore, it has a known triple companion on a relatively close orbit (Zasche et al. 2017). BAT 99-126 is a higher order system that contains an O-type contact system; however the orbital configuration of the system is not known so it is rejected (Janssens et al. 2021). HD 64315 is a quadruple system containing two pairs of close binaries, one of which is in a contact configuration. Unfortunately, the separation between the two pairs of binaries is not known so we do not include it in our sample (Lorenzo et al. 2017). Finally, UW CMa appears to be a contact system, but the light curve has some unexplained features in it that makes the fitting unreliable. So far, no reliable orbital solution has been found (Leung & Schneider 1978; Antokhina et al. 2011).

2.8. Photometric data preparation

While most of the photometric data used in this investigation were already reduced, some needed to be cleaned. Specifically, in the case where quality flags were provided, we removed all data points that had bad quality flags following the individual recommendations of each data set. For the data sets without quality flags, we removed obvious outliers.

In the case of TESS, only some of the objects in our sample had reduced light curves associated. While TESS is a nearly all sky survey, only some of the many stars observed have been reduced with the official TESS pipeline, SPOC (Jenkins et al. 2016). Of the six stars in our sample, only V382 Cyg and TU Mus have SPOC light curves, so for these objects we use the available light curves (see Fig. 2 as an example of the TESS light curve for V382 Cyg). For the four remaining sources, we utilize lightkurve (Lightkurve Collaboration 2018) to aid in the extraction.

lightkurve is a Python package designed for the retrieval and extraction of *Kepler*, K2, and TESS light curves. From the

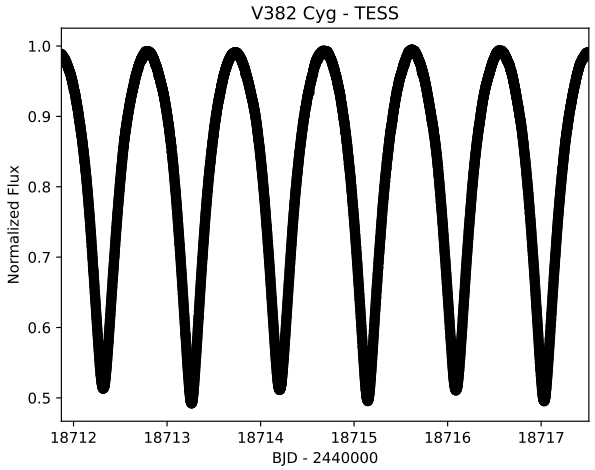

Fig. 2. Portion of the TESS light curve associated with V382 Cyg.

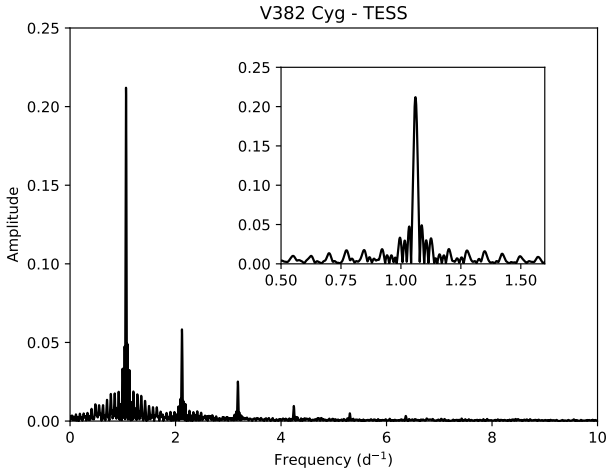

Fig. 3. Fourier spectrum of the TESS light curve associated with V382 Cyg. The inset shows a zoomed-in view around the dominant frequency. The other peaks visible in the periodogram correspond to harmonics of the fundamental frequency.

full frame image, we first created a 9×9 pixel cutout centered on the source in question (Brasseur et al. 2019). We then created a mask, which only includes the central pixel of the 9×9 cutout and generate a light curve from this mask. We chose to use only the central pixel in all cases to remain consistent between objects and sectors and to minimize the chances of contamination. VFTS 352 and SMC 108086 are located in crowded fields and given the TESS pixel size, eliminating contamination entirely is not possible. Since no additional periodicities were found in the light curves of these objects, and since we are only concerned with the period, the presence of third light in these objects is not problematic for our specific science case. Once the light curves were extracted, we removed NaNs and outliers, and we detrended the resulting light curve using the LIGHTKURVE flatten function. In some cases, there were trends at the beginning or end of the sectors as well as just before and after the mid sector downlinks. In these cases, we remove the spurious points.

3. Methods

3.1. Period determination with PERIOD04

In order to accurately determine the orbital period ($P_{\rm orb}$) from each photometric data set, we used the software package PERIOD04 (Lenz & Breger 2005). This tool, based on classical Fourier Analysis Techniques, is especially dedicated to the statistical analysis of large astronomical data sets containing gaps. Using PERIOD04, we computed the frequency spectrum of each light curve (see Fig. 3 as an example of the fourier spectrum of the TESS light curve for V382 Cyg) and identified the dominant periodicity in each data set. Since the orbital periods of our targets are known (see Table 1), we could easily determine if the dominant frequencies detected by the software were the true periods, a fraction/multiple of this, or a different periodicity present in the data. When the dominant frequency was not associated with the known period, we pre-whitened its contribution from the original data and continued extracting and pre-whitening frequencies until we could measure the period.

The uncertainties associated with each measured frequency were calculated by means of Monte Carlo simulations computed with PERIOD04. For each data set, we generated 1000 simulated time series with the times of observation matching those from the real data and the magnitudes (or intensities) were calculated from the magnitudes predicted by the best-fit plus Gaussian noise. For every time string, a least-squares calculation was performed and the frequency uncertainty was calculated from the distribution of the Monte Carlo results.

The frequency peaks associated with the orbital periods were easily identified in all data sets with signal-to-noise ratios ranging between five, for the shortest and most sparsely covered data sets, and ~40, for the frequency spectrum of the TESS light curves. For all data sets and all targets, the orbital frequencies that we found corresponded to double the true orbital frequencies, which is expected given the symmetry shown by overcontact binary light curves (see Fig. 2).

Since our data sets vary widely in both cadence and time base, we treat some data sets slightly differently than others. While the period determination process used is the same, some are split into smaller data subsets in order to avoid period smearing. For example, due to the long time base (~20 years) and sporadic nature of the observations, we split the INTEGRAL-OMC data sets in half and analyze each independently. Similarly, we treat data from OGLE II, III, and IV separately and determine independent periods for each. Finally, due to the biennial nature of the TESS mission, the TESS data set is divided by year.

3.2. Determination of the change in period ($\dot{P}$)

Once the periods associated with each data set were determined, we fit a linear regression through the data for each object to determine the overall change in period ($\dot{P}$). In some cases, multiple filters or apertures were observed simultaneously for a given data set (e.g., ASAS and ANDICAM), so to avoid unfairly weighing these data sets, we only include the aperture or filter that returned the lowest sigma from the period determination step in the linear fit. In the case of OGLE, since the *I* and *V* band observations were not taken simultaneously we include both as distinct data sets when available.

To avoid correlations between the two free parameters in the linear regression (namely the slope and the *y*-intercept), we offset the times such that a time of zero corresponds to the midpoint between the first and last central barycentric Julian Date (BJD) for each object. Here we define the central BJD of each data set as the midpoint of the observations. We optimized the two free parameters using the "curve_fit" function of the SCIPY package,

Table 2. Measured periods for each of the data subsets for each system in the sample and the resulting period change and period stability.

Object	Source	Central BJD (BJD – 2440000)	Period [d]	Period [s]	$\dot{P}$ [s yr^{-1}]	$P/\lvert\dot{P}\rvert$ [Myr]
LSS 3074	ANDICAM (V)	12015	2.1844 ± 0.0006	188730 ± 50	−0.7 ± 2.4	$0.27^{+\infty}_{-0.21}$
	ASAS (Ap3)	13483	2.185090 ± 0.000014	188791.8 ± 1.2		
	TESS (yr 1)	18610	2.1850 ± 0.0003	188780 ± 30		
	TESS (yr 3)	19347	2.1834 ± 0.0013	188650 ± 120		
MY Cam	M&V	14662	1.175476 ± 0.000004	101561.1 ± 0.3	−0.1 ± 0.6	$1.0^{+\infty}_{-0.8}$
	OMC (1/2)	14458	1.175427 ± 0.000006	101556.9 ± 0.5		
	OMC (2/2)	17770	1.175441 ± 0.000012	101558.1 ± 1.1		
	TESS (yr 2)	18828	1.17543 ± 0.00011	101557. ± 9.		
SMC 108086	OGLE II (I)	11250	0.883097 ± 0.000003	76299.6 ± 0.3	−0.11 ± 0.08	$0.7^{+2.1}_{-0.3}$
	OGLE III (I)	13529	0.883102 ± 0.000001	76300.04 ± 0.08		
	OGLE III (V)	14140	0.883084 ± 0.000003	76298.4 ± 0.2		
	OGLE IV (I)	16018	0.883089 ± 0.000003	76298.9 ± 0.2		
	OGLE IV (V)	16000	0.883103 ± 0.000014	76300.1 ± 1.2		
	TESS (yr 1)	18353	0.88306 ± 0.00002	76296. ± 2.		
	TESS (yr 3)	19060	0.88301 ± 0.00002	76292.4 ± 1.8		
TU Mus	HIPPARCOS	8411	1.387287 ± 0.000017	119861.6 ± 1.5	−0.005 ± 0.085	$25.4^{+\infty}_{-24.1}$
	OMC (1/2)	14443	1.387260 ± 0.000005	119859.3 ± 0.5		
	OMC (2/2)	17941	1.387290 ± 0.000005	119861.9 ± 0.5		
	ASAS (Ap3)	13527	1.387287 ± 0.000002	119861.6 ± 0.2		
	TESS (yr 1)	18596	1.387271 ± 0.000016	119860.3 ± 1.4		
	TESS (yr 3)	19333	1.387279 ± 0.000017	119860.9 ± 1.5		
V382 Cyg	HIPPARCOS	8452	1.88553 ± 0.00003	162910. ± 3.	0.01 ± 0.03	$16.5^{+\infty}_{-12.5}$
	OMC (1/2)	14163	1.885523 ± 0.000007	162909.2 ± 0.6		
	OMC (2/2)	17261	1.885525 ± 0.000005	162909.3 ± 0.5		
	TESS	18710	1.88554 ± 0.00003	162911. ± 2.		
VFTS 352	OGLE III (I)	13569	1.124167 ± 0.000001	97128.05 ± 0.10	−0.05 ± 0.10	$1.9^{+\infty}_{-1.2}$
	OGLE III (V)	13952	1.124154 ± 0.000005	97126.9 ± 0.5		
	OGLE IV (I)	15988	1.124151 ± 0.000001	97126.62 ± 0.12		
	OGLE IV (V)	15963	1.124162 ± 0.000003	97127.6 ± 0.3		
	TESS (yr 1)	18489	1.124195 ± 0.000005	97130.4 ± 0.4		
	TESS (yr 3)	19211	1.124172 ± 0.000006	97128.4 ± 0.5		

which utilizes nonlinear least squares to fit (Virtanen et al. 2020).

4. Results

Table 2 includes the central BJDs and orbital periods determined for each target from each independent data set together with their uncertainties. Additionally, Table 2 also lists the $\dot{P}$ and corresponding errors as well as the $P/|\dot{P}|$ for each object in our sample. An example of a more graphical representation of our results can be found in Fig. 4, which shows the measured periods for each of the data sets associated with V382 Cyg as well as the linear fit through these defining the $\dot{P}$. A similar figure for each of the other objects in our sample can be found in Appendix A.

In general, the measured periods were well constrained with small error bars (on the order of 1 second or less) and agreed with one another within a few seconds for each object, with two notable exceptions. In the case of LSS 3074, the errors on the period measurements were significantly larger than the rest of the sample by more than an order of magnitude, which in turn led to a larger error on the derived $\dot{P}$. The other notable exception is SMC 108086, which showed a small, but statistically significant downward trend over the time frame of the observations.

The measured $\dot{P}$ values for each object were all on the order of 0.1 s per year or less, with the exception of LSS 3074, which was about an order of magnitude higher. That being said, SMC 108086 was the only object in our sample whose $\dot{P}$ measurement was not consistent with zero within error. Calculating $P/|\dot{P}|$, we find that most of our sample has period variation timescales of ∼1 Myr or larger, while LSS 3074 shows a variation timescale of closer to 0.3 Myr. These values indicate that all objects in our sample are evolving on the nuclear timescale.

Several previous works have computed the period changes for some of the objects in our sample using various methods, and in general, we find a very good agreement between our measurements and previous measurements. In the case of V382 Cyg, there are a few independent period change measurements available in the literature (Değirmenci et al. 1999; Qian et al. 2007; Yaşarsoy & Yakut 2013), and all indicate a period increase of between ∼0.03 and 0.04 s per year, which agrees with our measurement within errors. For VFTS 352 the period change was never directly measured; however Almeida et al. (2015) reports a peak-to-peak period difference of ∼2 s over a 12.5 year time frame, which corresponds to an upper limit of $|\dot{P}| \leq 0.16$ s per year. This value is in good agreement with the upper limit that we measure of 0.15 s per year. Finally, TU Mus has one period change measurement in the literature from Qian et al. (2007), who measured $\dot{P} = 0.035$ s per year, which agrees nicely with our measurement within error.

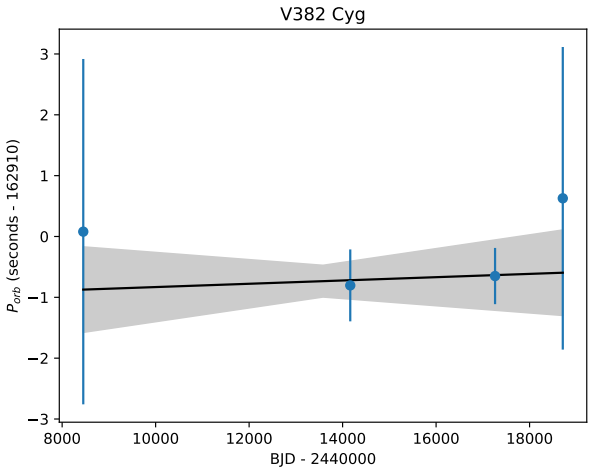

Fig. 4. Measured period as a function of time for V382 Cyg. The period is given in seconds, and the period associated with the first observation, rounded to the nearest second, is subtracted. A best-fit line is plotted in black, and its associated uncertainties are represented by the shaded region.

5. Discussion

In order to assess our theoretical understanding of the past and future evolution of massive overcontact systems, we compare our observations with population synthesis results adapted from Menon et al. (2021). This population synthesis was originally computed from a grid of binary models corresponding to the metallicity of the LMC. The original parameter space of the models spans an initial total mass of 20−80 $M_\odot$, initial period of P_i = 0.6−2 days and initial mass ratio of q_i = 0.6−1. Given that this current work focuses on O+O overcontact systems, we only consider models that have current primary and secondary masses $\geq$14 $M_\odot$ to compute the theoretical distribution of the observed parameters, namely P_orb, q and $\dot{P}$. The reader is referred to Menon et al. (2021) for a more detailed description of the population synthesis computations.

In general, we find that the models are able to reproduce the orbital parameters of the observed systems. However, based on Fig. 5, it is clear that the observed systems do not follow the expected distribution as determined via population synthesis. Almost all of the systems in the sample fall in low probability regions of the parameter space, indicating that these combinations of parameters are expected to be either very short-lived or rare.

A notable feature of the population synthesis results, which can be seen in Fig. 5 and the left panel of Fig. 6, is that the theoretical distribution for $P/|\dot{P}|$ peaks at around 100 Myr, which is longer than the expected main sequence lifetime for stars in this mass range. Given the fact that most of our measured $\dot{P}$ values are consistent with zero, we are unable to rule out this possibility; however, it is unlikely that these theoretical timescales are reliable. The large $P/|\dot{P}|$ values from the models are likely due to the way in which mass transfer is implemented during the contact phase in `MESA` (Paxton et al. 2015; Marchant et al. 2016). The mass transfer rate during the contact phase slows down to the order of 10^{-7} $M_\odot$ yr^{-1} as soon as q becomes close to one, after which, the mass ratio asymptotically approaches q = 1 until the system finally merges (Menon et al. 2021). This causes the models to spend the majority of their main-sequence lives with mass ratios close to one as reflected in the theoretical distributions. The observations on the other hand do not seem to support this, as the mass ratios are fairly well distributed between 0.6 and one.

Our observed mass ratio distribution is consistent with findings for lower mass contact systems as well, where low mass ratio contact systems are common (see, e.g., Yang & Qian 2015; Qian et al. 2020, and references therein). In studies of low mass convective core contact systems, observations have shown that the period stabilities are comparable to the values that we find here. Further, several systems have period changes suggesting that they are evolving toward a lower mass ratio rather than to one (Yang & Qian 2015).

Among the O+O models, we find that the main source of the q = 1 contact binaries are models with initial periods $P_\mathrm{i} \leq$ 1.2 days. If we only consider models with initial periods larger than 1.2 days, while the peak of the distribution still lies at q = 1, the distribution flattens considerably over the q dimension, and we begin to see a clear correlation between the mass ratio and the period stability (see Fig. 6). Interestingly; however, this correlation does not appear to be present in the observed distribution, suggesting that these systems may not equalize on the timescales that the models predict. That being said, these findings may suggest that the observed overcontact binaries originate from systems with longer initial periods (in line with findings from Ramírez-Tannus et al. 2017, 2021; Sana et al. 2017); however, a more dedicated theoretical investigation is needed to confirm this hypothesis.

While there appears to be a definite discrepancy between the observed population and the one predicted from population synthesis, there are several factors that should be considered before drawing conclusions:

First, we note that the models from Menon et al. (2021) are calculated assuming LMC metallicity, while most of our sample is Galactic. This difference in metallicity could affect the periods and period stabilities as massive stars at higher metallicities tend to have slightly larger radii and stronger winds at the same evolutionary stage, which may lead to shorter overall period stabilities.

Additionally, the population synthesis results assume systems that have an initial period of two days or less and assume that all mass transfer is conservative. Given that higher initial periods seem to allow for a more even q distribution, including initial periods of greater than two days in the population synthesis could allow for a better agreement between the population synthesis results and the observations.

Furthermore, the population synthesis results assume the systems have an initial mass ratio of greater than 0.6. As discussed in Menon et al. (2021), the likelihood of a system coming into contact, as well as the duration of the contact phase are strongly correlated with the initial mass ratio, implying that these systems would represent a small minority of the currently observable contact systems. That being said, the inclusion of systems with lower initial mass ratios may allow for a marginally better agreement between the population synthesis results and the observations.

An additional factor to consider is that the binary models do not include energy transfer. Considering the mass-radius relationship of single stars, as well as the strict relationship on their radii when a system is in contact, stable overcontact systems with a mass ratio away from unity would not be expected to exist theoretically (Kuiper 1941). However, as energy transfer is expected to occur in overcontact layers, the mass-radius relationship becomes dependent on the mass ratio and separation of the system, potentially allowing for stable solutions to exist (see, e.g., Shu et al. 1976). A detailed analysis on the impact of

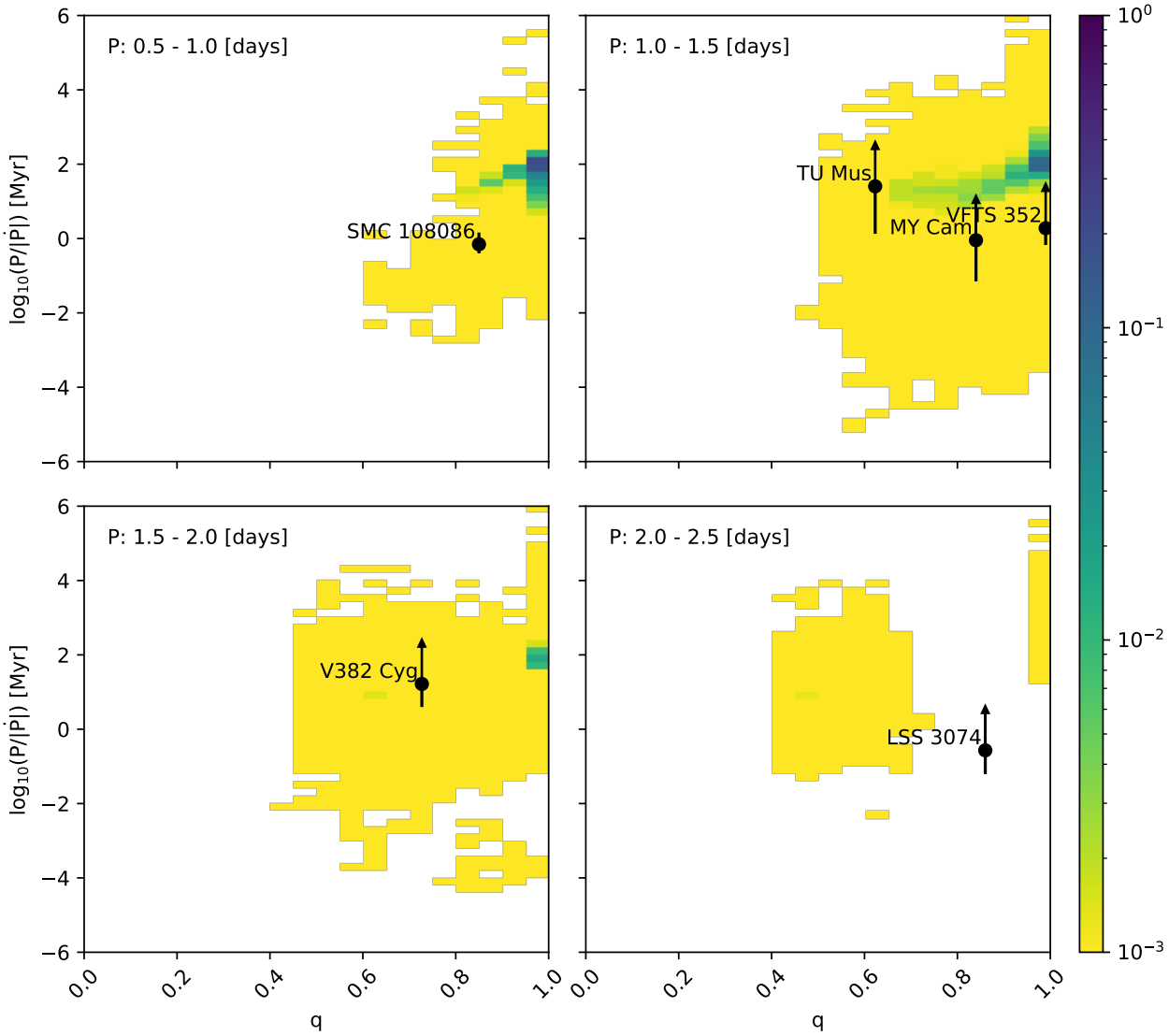

Fig. 5. Normalized theoretical probability distribution of the $P/|\dot{P}|$ as a function of the mass ratio based on models from Menon et al. (2021). The background color represents the probability of finding a system with the given combination of parameters. Lighter colors represent lower probabilities while darker colors represent higher probabilities. Each of the four panels represents a different period bin, which is indicated in the upper-left corner. The locations of the observed overcontact systems are indicated with black dots and labeled. Error bars are also plotted for each system and when applicable, arrows are used to indicate that the value does not have an upper limit.

energy transfer on populations of massive overcontact binaries has; however, not been done yet.

Finally, the implementation of the contact scheme itself in MESA, leads to the binary model spending an inordinately large amount of its contact lifetime close to a mass ratio of $q = 1$. This may indicate the requirement to improve the current contact scheme used in our models. While each of these assumptions will surely affect the final distribution, it is unlikely that the changes would be significant enough to rectify the discrepancy between the observations and the theoretical predictions. This could however account for the mass ratio gap that is seen in the bottom right panel of Fig. 5, and could perhaps allow the models to reproduce the location of LSS 3074.

One additional point to consider involves the comparison of the observed period stability with the theoretical values. As discussed in King & Lasota (2021), the measured $P/|\dot{P}|$ may be misleading on small timescales as changes in period can be caused by variations on the flow or temporary digressions from synchronicity. Over the long term, these fluctuations would average out, allowing a more robust comparison with theoretical models. We note, however that King & Lasota (2021) and studies like it (see, e.g., Pringle 1975) focus on ultra-luminous X-ray sources, where the primary stars are overflowing through L1, transferring mass to their companions. It is unlikely that overcontact systems would suffer from the same level of period variations as ultra-luminous X-ray sources given that overcontact systems are expected to be in hydrostatic equilibrium and rotating synchronously. Nevertheless, comparing the $P/|\dot{P}|$ of the complete sample of O+O overcontact systems as a whole instead of individual sources allows us to circumvent this potential issue.

6. Conclusions

We have performed a period stability study of known O+O type overcontact systems. Using archival photometric data and the software package PERIOD04, we calculated the periods of the systems over a time span of tens of years. For each system in our sample, we determined the rate at which the period is changing

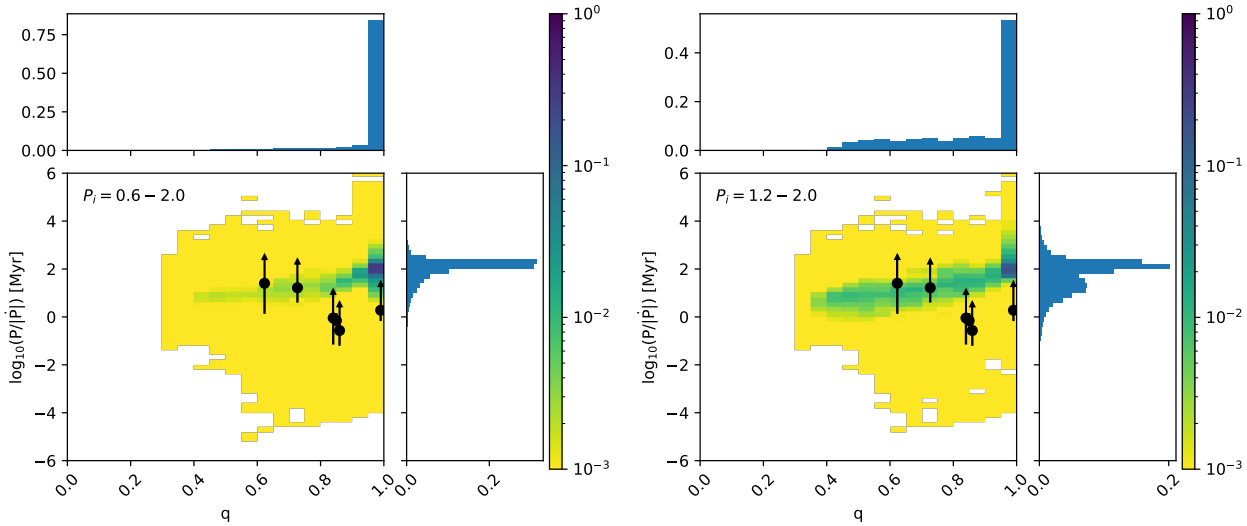

Fig. 6. Same as Fig. 5 but for different initial period ranges: $P_i = 0.6-2.0$ and $P_i = 1.2-2.0$ for the *left and right panels*, respectively. Additionally, 1D histograms corresponding to each of the axes are plotted.

via a linear regression through the period measurements of each data subset. We find that all systems in our sample show period changes consistent with zero with the exception of SMC 108086, which shows a slight but non-negligible negative period change. These results indicate that all of the systems in our sample have periods that are stable on the nuclear timescale. Furthermore, we find no correlation between the mass ratio and the period stability, which implies that these systems will continue to evolve as unequal-mass overcontact binaries.

Comparing our results with population synthesis simulations, we find discrepancies between the predicted and observed distributions. While the population synthesis simulations predict that the overwhelming majority of overcontact systems should be found in equal-mass systems, the mass ratios of the observed systems are fairly evenly distributed between $q = 0.6$ and 1. This discrepancy is marginally lessened by removing the shortest period systems in the population synthesis simulations, suggesting that the observed population of overcontact systems may have originated from binaries with longer initial periods. A more in-depth theoretical investigation is needed to confirm this; however. That being said, without a larger sample size, it is difficult to draw strong conclusions, which highlights the need for a dedicated effort to search for and characterize currently undiscovered massive overcontact systems.

Acknowledgements. This paper includes data collected by the TESS mission, which are publicly available from the Mikulski Archive for Space Telescopes (MAST). Funding for the TESS mission is provided by NASA's Science Mission directorate. This research made use of Lightkurve, a Python package for Kepler and TESS data analysis (Lightkurve Collaboration 2018). A.M. would like to thank the Alexander von Humboldt foundation for supporting this project. L.M. thanks the European Space Agency (ESA) and the Belgian Federal Science Policy Office (BELSPO) for their support in the framework of the PRODEX Programme. P.M. acknowledges support from the FWO junior postdoctoral fellowship No. 12ZY520N

References

Abdul-Masih, M., Sana, H., Sundqvist, J., et al. 2019, ApJ, 880, 115
Abdul-Masih, M., Sana, H., Conroy, K. E., et al. 2020, A&A, 636, A59
Abdul-Masih, M., Sana, H., Hawcroft, C., et al. 2021, A&A, 651, A96
Alfonso-Garzón, J., Domingo, A., Mas-Hesse, J. M., & Giménez, A. 2012, A&A, 548, A79
Almeida, L. A., Sana, H., de Mink, S. E., et al. 2015, ApJ, 812, 102
Almeida, L. A., Sana, H., Taylor, W., et al. 2017, A&A, 598, A84
Andersen, J., & Grønbech, B. 1975, A&A, 45, 107
Antokhina, E. A., Srinivasa Rao, M., & Parthasarathy, M. 2011, New Astron., 16, 177
Antokhina, E. A., Kumsiashvili, M. I., & Chargeishvili, K. B. 2016, Astrophysics, 59, 68
Brasseur, C. E., Phillip, C., Fleming, S. W., et al. 2019, Astrophysics Source Code Library [record ascl:1905.007]
Burkholder, V., Massey, P., & Morrell, N. 1997, ApJ, 490, 328
Cester, B., Fedel, B., Giuricin, G., Mardirossian, F., & Mezzetti, M. 1978, A&AS, 33, 91
de Mink, S. E., & Mandel, I. 2016, MNRAS, 460, 3545
de Mink, S. E., Pols, O. R., & Hilditch, R. W. 2007, A&A, 467, 1181
Değirmenci, Ö. L., Sezer, C., Demircan, O., et al. 1999, A&AS, 134, 327
du Buisson, L., Marchant, P., Podsiadlowski, P., et al. 2020, MNRAS, 499, 5941
Duchêne, G., & Kraus, A. 2013, ARA&A, 51, 269
Eggen, O. J., & Iben, I., Jr 1989, AJ, 97, 431
Fabry, M., Marchant, P., & Sana, H. 2022, A&A, 661, A123
Harries, T. J., Hilditch, R. W., & Hill, G. 1997, MNRAS, 285, 277
Hilditch, R. W., Howarth, I. D., & Harries, T. J. 2005, MNRAS, 357, 304
Janssens, S., Shenar, T., Mahy, L., et al. 2021, A&A, 646, A33
Jenkins, J. M., Twicken, J. D., McCauliff, S., et al. 2016, in Software and Cyberinfrastructure for Astronomy IV, eds. G. Chiozzi, & J. C. Guzman, SPIE Conf. Ser., 9913, 99133E
Justham, S., Podsiadlowski, P., & Vink, J. S. 2014, ApJ, 796, 121
King, A., & Lasota, J. P. 2021, ArXiv e-prints [arXiv:2112.03779]
Kozai, Y. 1962, AJ, 67, 591
Kuiper, G. P. 1941, ApJ, 93, 133
Langer, N., Schürmann, C., Stoll, K., et al. 2020, A&A, 638, A39
Lenz, P., & Breger, M. 2005, Commun. Asteroseismol., 146, 53
Leung, K. C., & Schneider, D. P. 1978, ApJ, 222, 924
Lidov, M. L. 1962, Planet Space Sci., 9, 719
Lightkurve Collaboration (Cardoso, J. V. D. M., et al.) 2018, Astrophysics Source Code Library [record ascl:1812.013]
Linder, N., Rauw, G., Sana, H., De Becker, M., & Gosset, E. 2007, A&A, 474, 193
Lorenzo, J., Negueruela, I., Baker, A. K. F. V., et al. 2014, A&A, 572, A110
Lorenzo, J., Simón-Díaz, S., Negueruela, I., et al. 2017, A&A, 606, A54
Mahy, L., Almeida, L. A., Sana, H., et al. 2020a, A&A, 634, A119
Mahy, L., Sana, H., Abdul-Masih, M., et al. 2020b, A&A, 634, A118
Maíz Apellániz, J., Sota, A., Arias, J. I., et al. 2016, ApJS, 224, 4
Mandel, I., & de Mink, S. E. 2016, MNRAS, 458, 2634
Marchant, P., Langer, N., Podsiadlowski, P., Tauris, T. M., & Moriya, T. J. 2016, A&A, 588, A50
Martins, F., Mahy, L., & Hervé, A. 2017, A&A, 607, A82
Mateo, M., Harris, H. C., Nemec, J., & Olszewski, E. W. 1990, AJ, 100, 469
Menon, A., & Heger, A. 2017, MNRAS, 469, 4649
Menon, A., Langer, N., de Mink, S. E., et al. 2021, MNRAS, 507, 5013
Mochnacki, S. W., & Doughty, N. A. 1972, MNRAS, 156, 51
Moe, M., & Di Stefano, R. 2017, ApJS, 230, 15

Pawlak, M., Soszyński, I., Udalski, A., et al. 2016, Acta Astron., 66, 421
Paxton, B., Marchant, P., Schwab, J., et al. 2015, ApJS, 220, 15
Penny, L. R., Ouzts, C., & Gies, D. R. 2008, ApJ, 681, 554
Perryman, M. A. C., Lindegren, L., Kovalevsky, J., et al. 1997, A&A, 323, L49
Podsiadlowski, P., Joss, P. C., & Hsu, J. J. L. 1992, ApJ, 391, 246
Pojmanski, G. 1997, Acta Astron., 47, 467
Pojmanski, G. 2002, Acta Astron., 52, 397
Pojmanski, G. 2003, Acta Astron., 53, 341
Pojmanski, G., & Maciejewski, G. 2004, Acta Astron., 54, 153
Pojmanski, G., & Maciejewski, G. 2005, Acta Astron., 55, 97
Pojmanski, G., Pilecki, B., & Szczygiel, D. 2005, Acta Astron., 55, 275
Pols, O. R. 1994, A&A, 290, 119
Popper, D. M. 1978, ApJ, 220, L11
Popper, D. M., & Hill, G. 1991, AJ, 101, 600
Pringle, J. E. 1975, MNRAS, 170, 633
Qian, S. B., Yuan, J. Z., Liu, L., et al. 2007, MNRAS, 380, 1599
Qian, S.-B., Zhu, L.-Y., Liu, L., et al. 2020, Res. Astron. Astrophys., 20, 163
Ramírez-Tannus, M. C., Kaper, L., de Koter, A., et al. 2017, A&A, 604, A78
Ramírez-Tannus, M. C., Backs, F., de Koter, A., et al. 2021, A&A, 645, L10
Raucq, F., Gosset, E., Rauw, G., et al. 2017, A&A, 601, A133
Ricker, G. R., Winn, J. N., Vanderspek, R., et al. 2015, J. Astron. Telesc. Instrum. Syst., 1, 014003
Riley, J., Mandel, I., Marchant, P., et al. 2021, MNRAS, 505, 663
Sana, H., & Evans, C. J. 2011, in Active OB Stars: Structure, Evolution, Mass Loss, and Critical Limits, eds. C. Neiner, G. Wade, G. Meynet, & G. Peters, 272, 474
Sana, H., de Mink, S. E., de Koter, A., et al. 2012, Science, 337, 444
Sana, H., Ramírez-Tannus, M. C., de Koter, A., et al. 2017, A&A, 599, L9
Schneider, F. R. N., Ohlmann, S. T., Podsiadlowski, P., et al. 2019, Nature, 574, 211
Shao, Y., & Li, X.-D. 2014, ApJ, 796, 37
Shu, F. H., Lubow, S. H., & Anderson, L. 1976, ApJ, 209, 536
Smith, N., Andrews, J. E., Rest, A., et al. 2018, MNRAS, 480, 1466
Sota, A., Maíz Apellániz, J., Morrell, N. I., et al. 2014, ApJS, 211, 10
Stickland, D. J., Koch, R. H., Pachoulakis, I., & Pfeiffer, R. J. 1994, Observatory, 114, 107
Stickland, D. J., Lloyd, C., Koch, R. H., & Pachoulakis, I. 1995, Observatory, 115, 317
Szymanski, M. K. 2005, Acta Astron., 55, 43
Terrell, D., Munari, U., Zwitter, T., & Nelson, R. H. 2003, AJ, 126, 2988
Toonen, S., Hamers, A., & Portegies Zwart, S. 2016, Comput. Astrophys. Cosmol., 3, 6
Udalski, A., Kubiak, M., & Szymanski, M. 1997, Acta Astron., 47, 319
Udalski, A., Szymanski, M. K., Soszynski, I., & Poleski, R. 2008, Acta Astron., 58, 69
Udalski, A., Szymański, M. K., & Szymański, G. 2015, Acta Astron., 65, 1
Urushibata, T., Takahashi, K., Umeda, H., & Yoshida, T. 2018, MNRAS, 473, L101
Virtanen, P., Gommers, R., Oliphant, T. E., et al. 2020, Nat. Methods, 17, 261
von Zeipel, H. 1910, Astron. Nachr., 183, 345
Walborn, N. R., Sana, H., Simón-Díaz, S., et al. 2014, A&A, 564, A40
Wellstein, S., Langer, N., & Braun, H. 2001, A&A, 369, 939
Yaşarsoy, B., & Yakut, K. 2013, AJ, 145, 9
Yang, Y.-G., & Qian, S.-B. 2015, AJ, 150, 69
Zasche, P., Wolf, M., & Vraštil, J. 2017, MNRAS, 472, 2241
Zhao, E., Qian, S., Li, L., et al. 2014, New Astron., 26, 112

Appendix A: Period plots

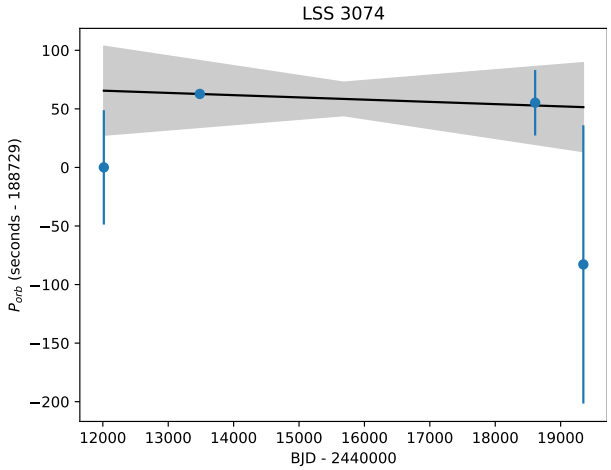

Fig. A.1. Same as Fig. 4 but for LSS 3074.

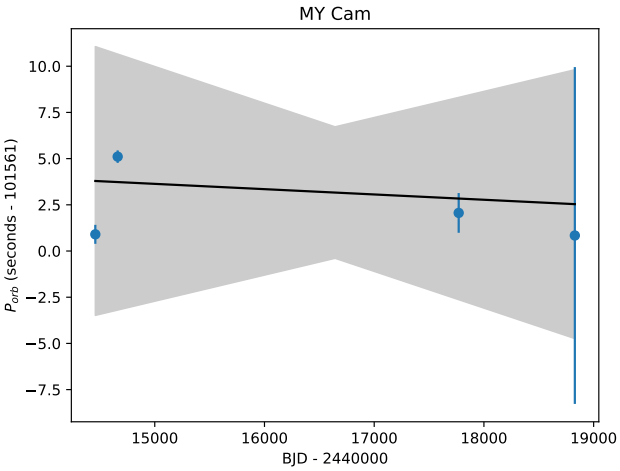

Fig. A.2. Same as Fig. 4 but for MY Cam.

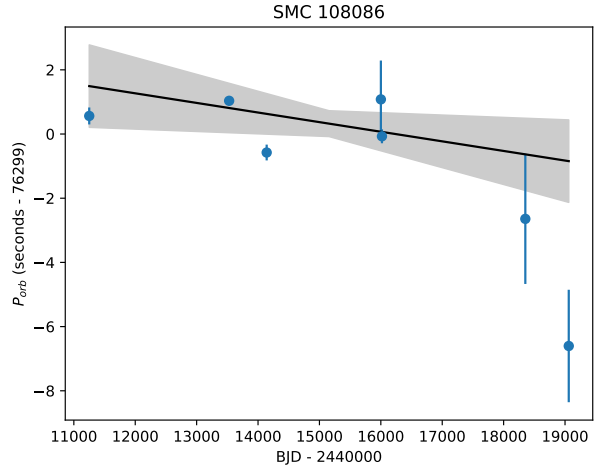

Fig. A.3. Same as Fig. 4 but for SMC 108086.

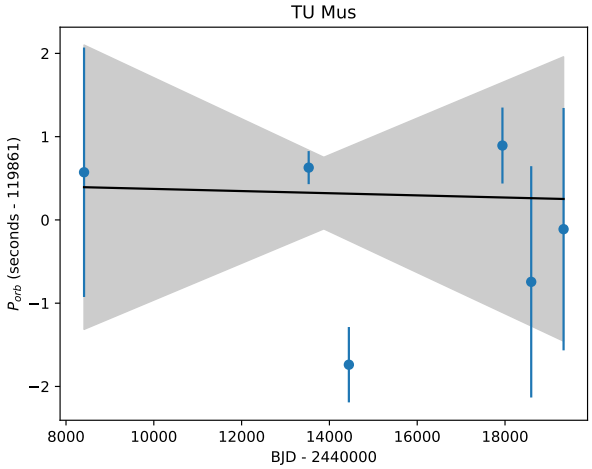

Fig. A.4. Same as Fig. 4 but for V382 Cyg.

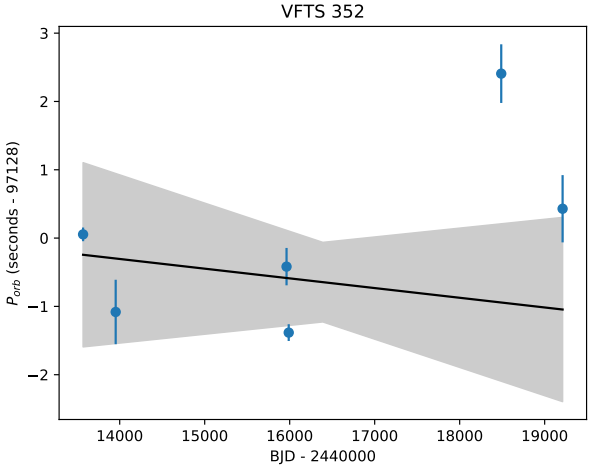

Fig. A.5. Same as Fig. 4 but for VFTS 352.